The structure of the torque ring of the flagellar motor and the molecular basis for rotational switching

Lawrence K. Lee[1], Michael A. Ginsburg[1], Claudia Crovace[2], Mhairi Donohoe[1] & Daniela Stock[1,3]

Materials and Methods

The full length FliG protein from *A. aeolicus* was expressed with an N-terminal cleavable Glutathion-S-transferase tag (GST-tag) and purified using a GSTrap HP column (GE Healthcare). The GST-tag was then removed with 6xHis-TEV protease. The protein mixture was passed through HisTrap and GSTrap columns (GE Healthcare) to remove TEV protease and GST, respectively. The flow through containing FliG protein was concentrated and passed over a superdex 200 column (GE Healthcare) equilibrated in 20 mM Tris/Cl pH 7.4, 100 mM NaCl and eluted as a single peak at the expected size of a FliG monomer. Peak fractions were pooled and concentrated to 10 mg/ml. The protein was crystallised at 20°C in Cryschem sitting drop vapour diffusion plates (Hampton Research) with a precipitant containing 45% 1,4 butanediol and 0.1 M Tris-Acetate pH 8.75. Crystals were flash-frozen in liquid nitrogen and a native data set was collected at beamline ID14-1 at the European Synchrotron Radiation Facility in Grenoble, France. Data were processed with MOSFLM[31] and SCALA[32] (see Supplementary Table 1). Attempts to solve the structure using *T. maritima* $FliG_{MC}$ coordinates as a template for molecular replacement were unsuccessful. Instead, crystals were grown using selenomethionine-substituted protein and data were collected at three different wavelengths at beamline 14-ID-B at APS, Chicago, U.S.A.

Selenomethionine containing protein was over-expressed in *E. coli* B834 (DE3) cells (Novagen) with selenomethionine-containing media[33] and purified as described above, except that 10 mM β-mercaptoethanol was added to all buffers. Selenomethionine containing crystals were grown under the same conditions as native crystals, except that 2 mM β-mercaptoethanol was added and the drops were micro-seeded with seeds from native crystals. Initial phases were obtained by combining SAD data from three isomorphous crystals containing selenomethionine-substituted protein (see Supplementary Table 1). The heavy atom positions were determined with SHELX[34] and refined with SHARP[35]. Rounds of model building with Coot[36] and refinement with REFMAC5[32] produced a complete model, which was used to phase the native data set to 2.4 Å resolution. This was refined with REFMAC and PHENIX[37] in several cycles iterating with model building (see Supplementary Table 2). The refined structure was assessed with MolProbity[38]. Partial charges were calculated with PDB2PQR[39] and the Poisson-Boltzmann equation was solved using the APBS module of the VMD molecular graphics software[40]. Morphs and intermediate states were generated by interpolating phi and psi angles in putative hinge loop regions.

Supplementary Tables and Figures

Supplementary Table 1. Data collection statistics

	Selenomethionine (3 crystals)	Native
Wavelength (Å)	0.97957 (Se-edge)	0.93400
Spacegroup	$P2_1$	$P2_1$
Cell dimensions (Å)	a=60.4,b=66.1,c=68.0, β=109.4°	a=60.0,b=65.8,c=67.8, β=110°
Resolution (Å)	33.2 – 2.65 (2.79 – 2.65)	65.0 – 2.40 (2.53 – 2.4)
Observed reflections	475280	178666
Unique reflections	14773	19453
Completeness (%)	99.5 (100)	98.8 (100)
Anomalous completeness	99.3 (100)	
Multiplicity	5.9 (5.9)	3.6 (3.6)
Mean I/sigma(I)	17.3 (2.3)	15.4 (4.1)
R_{merge} (%)	14.4 (117)	5.4 (33.8)

* values for the highest resolution shell are shown in parenthesis

Supplementary Table 2. X-ray refinement statistics

Resolution (Å)	20.0 - 2.40
R_{work}/R_{free}	21.6%/27.0%
Number of atoms	
Protein (non hydrogens)	2567
Water	32
Mean B-value (Å^2)	52.9
R.m.s deviations	
Bond lengths (Å)	0.01
Bond angles (°)	1.07
Ramachandran statistics	
Most favoured (%)	98
Additionally allowed (%)	1.7
Generously allowed (%)	0.3
Disallowed (%)	0.0

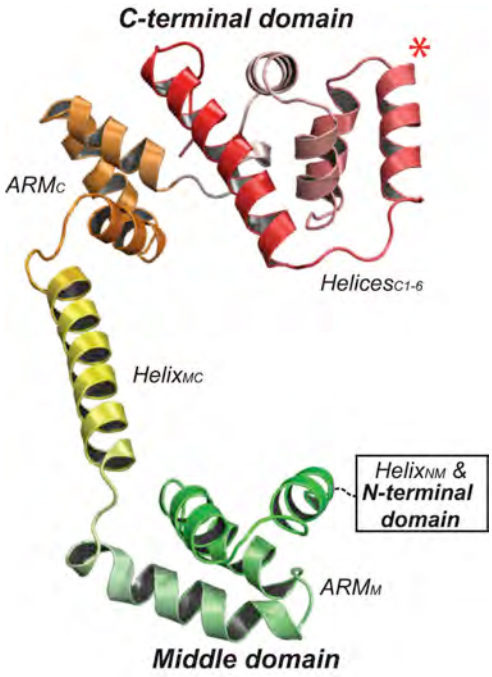

Supplementary Figure 1. The overall structure of $FliG_{MC}$ is shown in the same colour scheme and with ARM_M in the same orientation as $FliG_{FL}$ in Fig. 1a. Torque $helix_{C5}$ is labelled with a red asterisk.

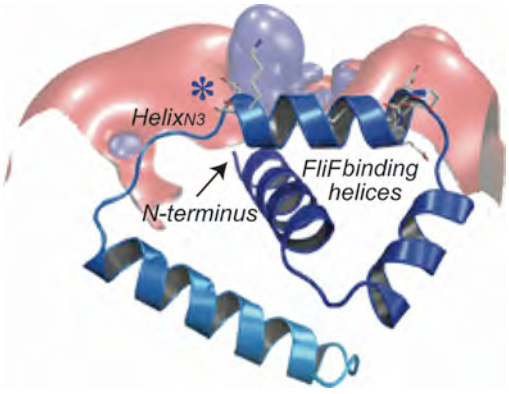

Supplementary Figure 2. Electrostatic surface potential around $helix_{N3}$ of the N-terminal domain contoured at ± 2.57 mV, as in Fig. 1b. Although the sequence of $helix_{N3}$ shows sequence homology to the torque $helix_{C5}$, it lacks the distinctive polar electrostatic charge distribution.

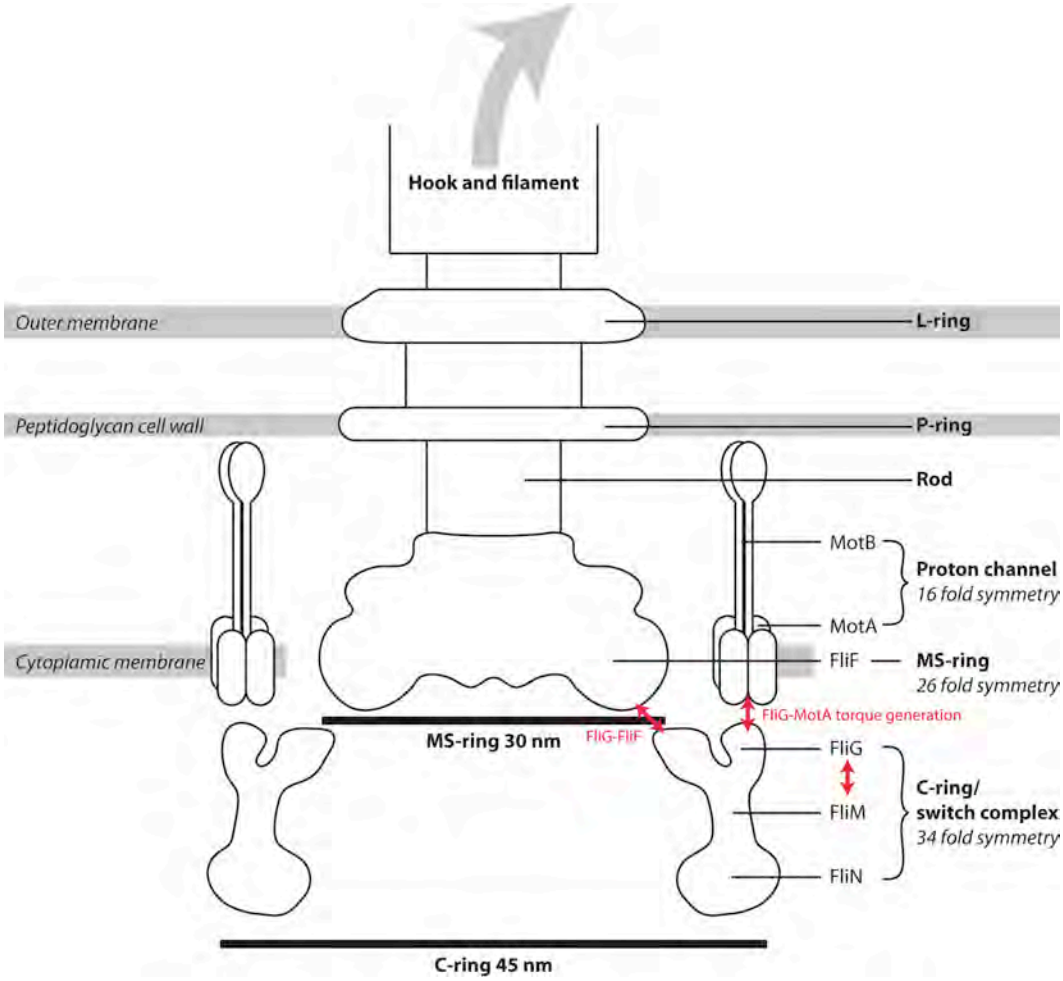

Supplementary Figure 3. Schematic diagram of the architecture of the flagellar motor. Gross structural features are labelled in bold on the right hand side. At their approximate locations, the proteins that comprise the C ring, MS ring and the stator complexes are labelled as well as the observed symmetry from 3D EM reconstructions. The interaction between FliG and FliF, MotA and FliM are marked with red arrows and labelled.

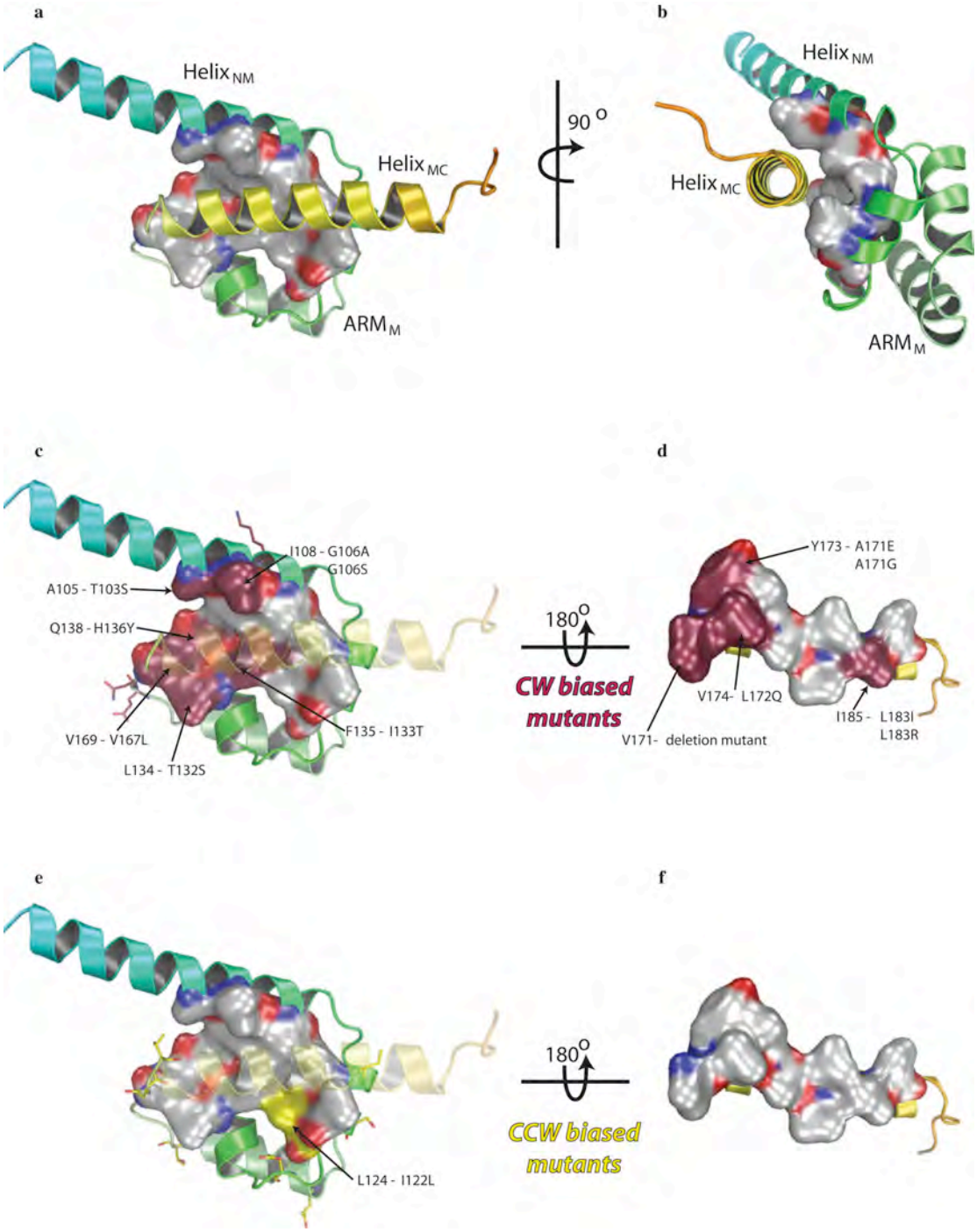

Supplementary Figure 4. CW and CCW biased mutations around the hydrophobic interface between helix$_{MC}$ and ARM$_{M}$. Mutants on the interfacial surfaces are from *S. typhimurium* and labelled with the residue from the crystal structure (left) and the equivalent mutations in *S. typhimurium* (right). The top (**a**) and side (**b**) view of the middle domain from FliG$_{FL}$ (*'closed'*

conformation) are displayed with the hydrophobic interface on ARM_M rendered as a surface. **c**, the same view as (**a**) and rotated 180° in (**d**), where the interfacial surface on $helix_{MC}$ is shown. CW-biased mutants are coloured in maroon. **e** and **f**, display the same views as (**c**) and (**d**) respectively, except with CCW-biased mutants coloured in yellow.

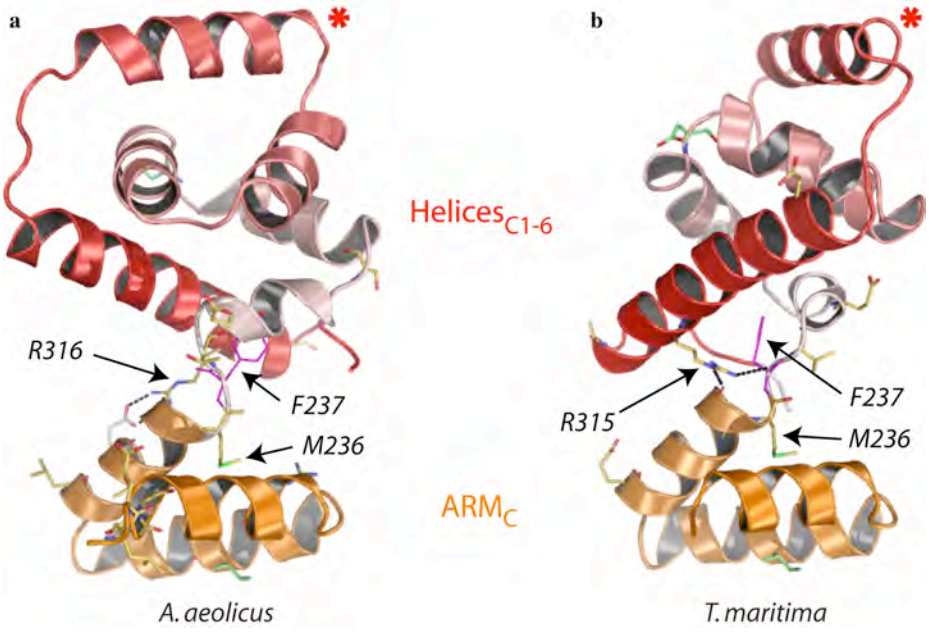

Supplementary Figure 5. Rotationally biased mutants in the C-terminal domain of $FliG_{FL}$ (**a**) and $FliG_{MC}$ (**b**) are shown as orange (CW) or green (CCW) sticks. F237 (magenta) and M236 that form the hinge that mediates the transition between the two structures are labelled. Torque $helix_{C5}$ is labelled with a red asterisk.

Rotationally biased mutants in the C-terminal domain can affect the relative orientation of ARM_C and $helices_{C1-6}$ suggesting that the conformational plasticity in the C-terminal domain is also involved in rotational switching. These mutations occur at 14 different positions and a majority of these are

between ARM_C and $helices_{C1-6}$[8,18,19,23]. Some appear to be able to influence the conformational state, however it is unclear whether they favour one conformation over the other. For example, one CW-biased mutation is a conservative substitution of M236 to an isoleucine residue[8]. M236 forms the centre of the hydrophobic core of the ARM_C motif and F237 forms part of the hydrophobic core of $helices_{c1-6}$. Consequently the relative movement of the two domains is largely restricted to changes in either the M236 psi or F237 phi torsion angles that lie between these side chains. The flexibility of the M236 side chain allows for the 25.6° difference in M236 phi between $Cter_{FL}$ and $Cter_{MC}$, without disrupting the structure of ARM_M, whereas a more rigid isoleucine residue would be more restrictive. Thus, the CW biased nature of the M236I mutant suggests that changes in M236 phi are associated with rotational switching. Another CW biased mutant occurs at the highly conserved residues R313 from *S. typhimurium*[8]. The equivalent residues in *A. aeolicus* and *T. maritima*, (R316 and R315 respectively) form hydrogen bonds that bridge the two subdomains (ARM_M and $helices_{C1-6}$).

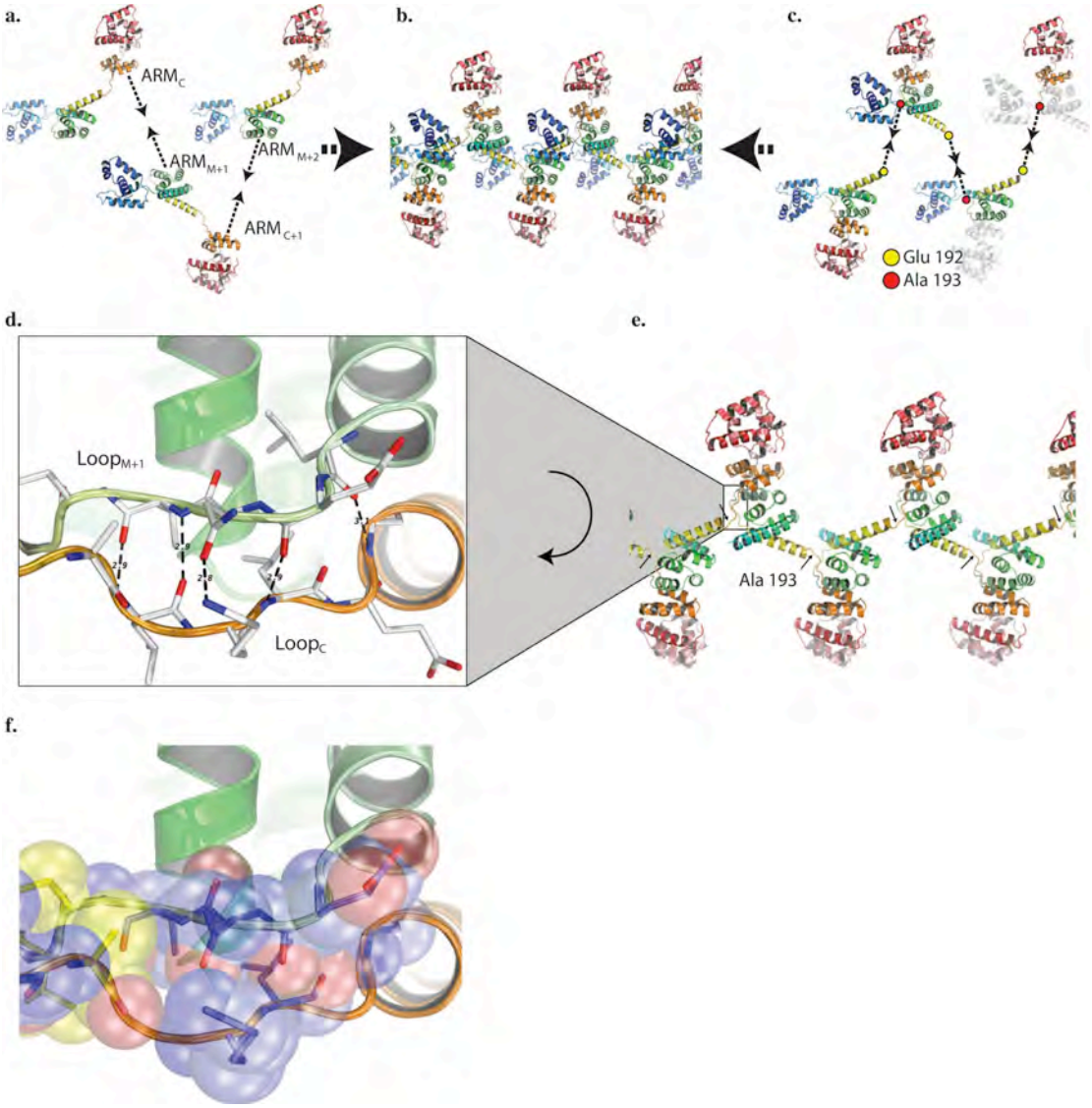

Supplementary Figure 6. The arrangement of structural features in the FliG multimer from the FliG$_{FL}$ crystal lattice. **a**, illustrates the organisation of FliG monomers in the crystal multimer (**b**) and (**c**) illustrate the arrangement of FliG$_{UNIT}$s in the crystal lattice. Here, E192 and A193 are shown in yellow and red spheres respectively. **d**, close up view of the intermolecular β-sheet that is formed between adjacent monomers. Hydrogen bonds between strands and their lengths (Å) are displayed. **e**, the crystal multimer is displayed without the N-terminal domain. A193 is labelled with arrows to illustrate how it is not constrained by secondary structure and may confer a degree of flexibility to

the multimer. The intermolecular β-sheet is encircled. **f**, the equivalent residues where mutations can bias rotation on the intermolecular β-sheet are shown as blue sticks with transparent spheres.

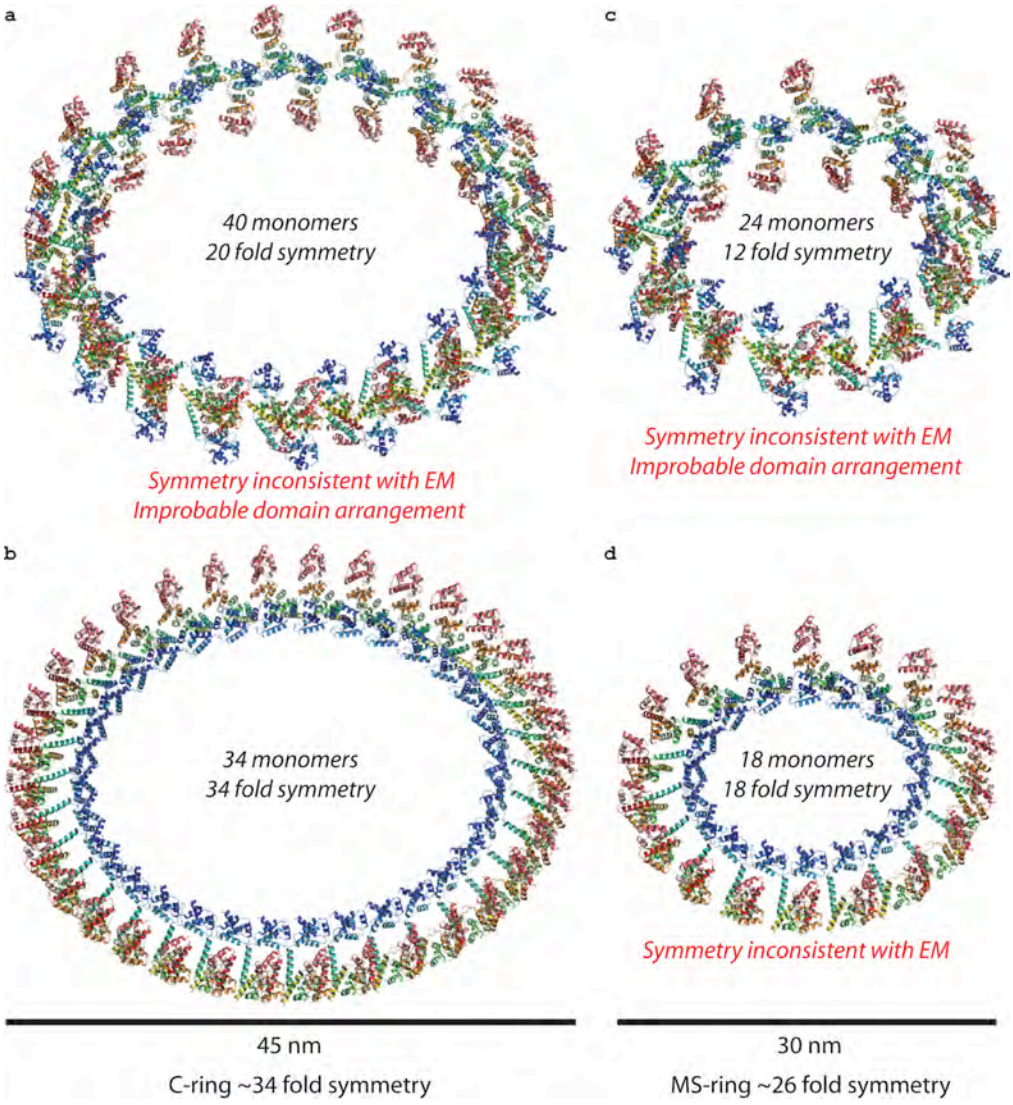

Supplementary Figure 7. Alternative arrangements of FliG rings. 40 or 34 $FliG_{UNIT}$s are required to span the circumference of a ring with a 45 nm diameter, when adjacent protomers are in opposite (**a**) or the same (**b**) orientations respectively. **a**, The alternating orientations give rise to a 20-fold symmetry, which is inconsistent with the observed symmetry in the C-ring. **b**, In contrast, when protomers are in the same orientation, their symmetry

matches the 34-fold symmetry in the C-ring. Furthermore, alternating orientations of $FliG_{UNIT}$s are not consistent with EM micrographs that indicate that FliF and the MotA stators that interact with the N and C-terminal domains of FliG are localised to one side of the FliG ring on the inner and outer periphery respectively. This spatial restraint is satisfied when all $FliG_{UNIT}$s are in the same orientation (**b**). Previous work reported a marginal thickening on the cytoplasmic side of the MS-ring that is integrated into the cytoplasmic membrane (see Supplementary Fig. 3), which could be decorated with anti-FliG antibody[15,41]. This line of evidence suggests that FliG sits on the cytoplasmic face of the MS-ring. We generated FliG rings with a 30 nm diameter with $FliG_{UNIT}$s in alternating (**c**) and the same (**d**) orientations. These exhibited 12 and 18-fold symmetry respectively, but neither of them is consistent with the observed 26-fold symmetry of the MS ring.

E. coli containing a FliG-FliF fusion mutant produce fully assembled flagellar motors with only subtle differences to wild-type[28], suggesting that FliG binds to FliF in a 1:1 ratio. However, FliF forms the MS-ring that has an apparent 26-fold symmetry[25,41]. Further, 26 substeps per revolution were observed during CCW rotation[42]. Equally though, *in situ* cryo-electron tomograms indicate that the MotA/B stator interacts with FliG in the C-ring that has a 34-fold symmetry[29,30,43] and 35 substeps were observed during CW rotation[42]. While it is beyond the scope of this study to solve this problem, which can only be resolved by a high resolution structure of the intact FliF-FliG ring, one possible explanation could be that the symmetry of the MS-ring may not necessarily reflect the number of FliF subunits in the ring. This argument is supported by recent 3D EM tomography of the flagellar motor from *B.*

burgdorferi, that exhibits a clear 16-fold symmetry in a larger MS-ring with a diameter of 50 nm[29], yet the MS-ring from *S. typhimurium* has a diameter of 30 nm but a 26-fold symmetry[25]. It is highly unlikely that far fewer FliF subunits could form a significantly larger ring.

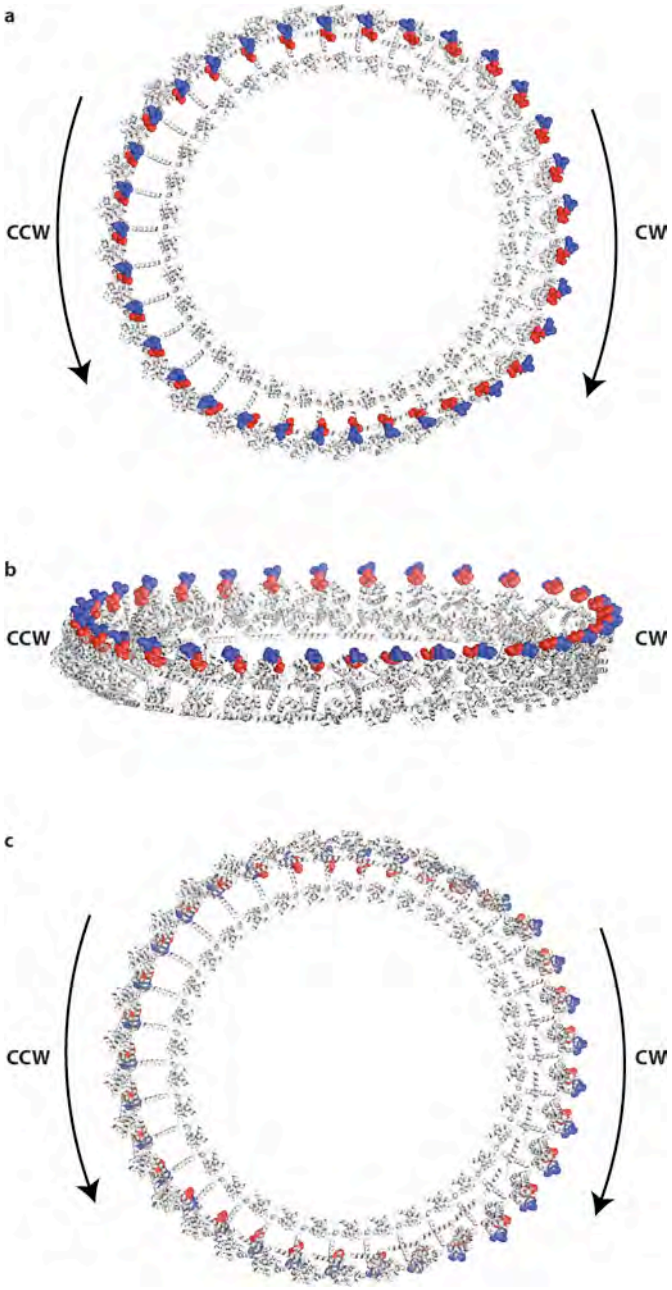

Supplementary Figure 8. A FliG ring displaying opposing switch states viewed from the top (**a**), side (**b**) and bottom (**c**). Protomers on the right side of the rings

are in a CW state whereas protomers on the left side are in a CCW state. The model allows for this to occur without compromising stereochemistry by bridging the opposing conformations with an interpolation of protomers in intermediate states.

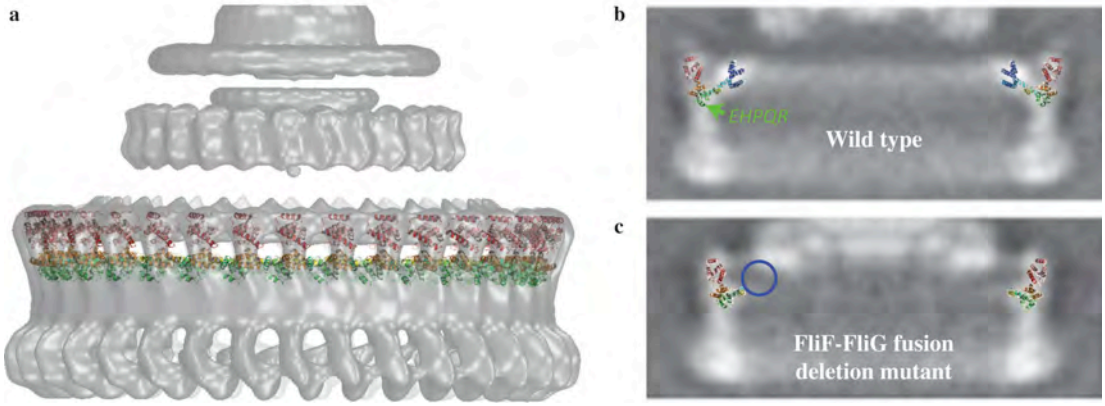

Supplementary Figure 9. Docking of the CW FliG ring into the 3D EM reconstruction of the CW-locked mutant of the flagellar motor[25] from *S. typhimurium*. **a**, the main body of the $FliG_{UNIT}$s (ARM superhelix and $helices_{C1-6}$) in the ring are shown docked into the EM density at the top of the C-ring. The vertical cross-section of the FliG ring is shown superimposed onto EM micrographs of the vertical cross-section of the *S. typhimurium* flagellar motor basal body from wild-type (**b**) and the FliG-FliF deletion mutant (**c**), which is missing the first 94 residues of FliG. EM densities in **b**, and **c**, were reproduced with permission from the American Society for Microbiology.

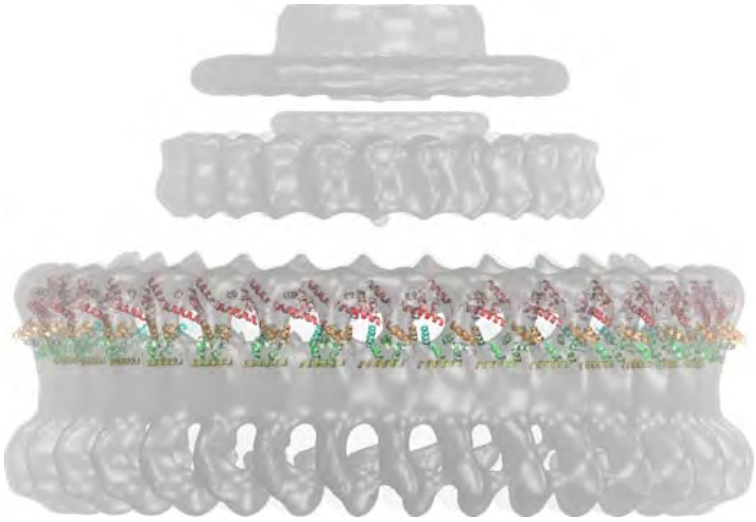

Supplementary Figure 10. Docking of the CCW FliG ring into the 3D EM reconstruction of the CW-locked mutant of the flagellar motor[25] from *S. typhimurium* illustrating the poor fit.

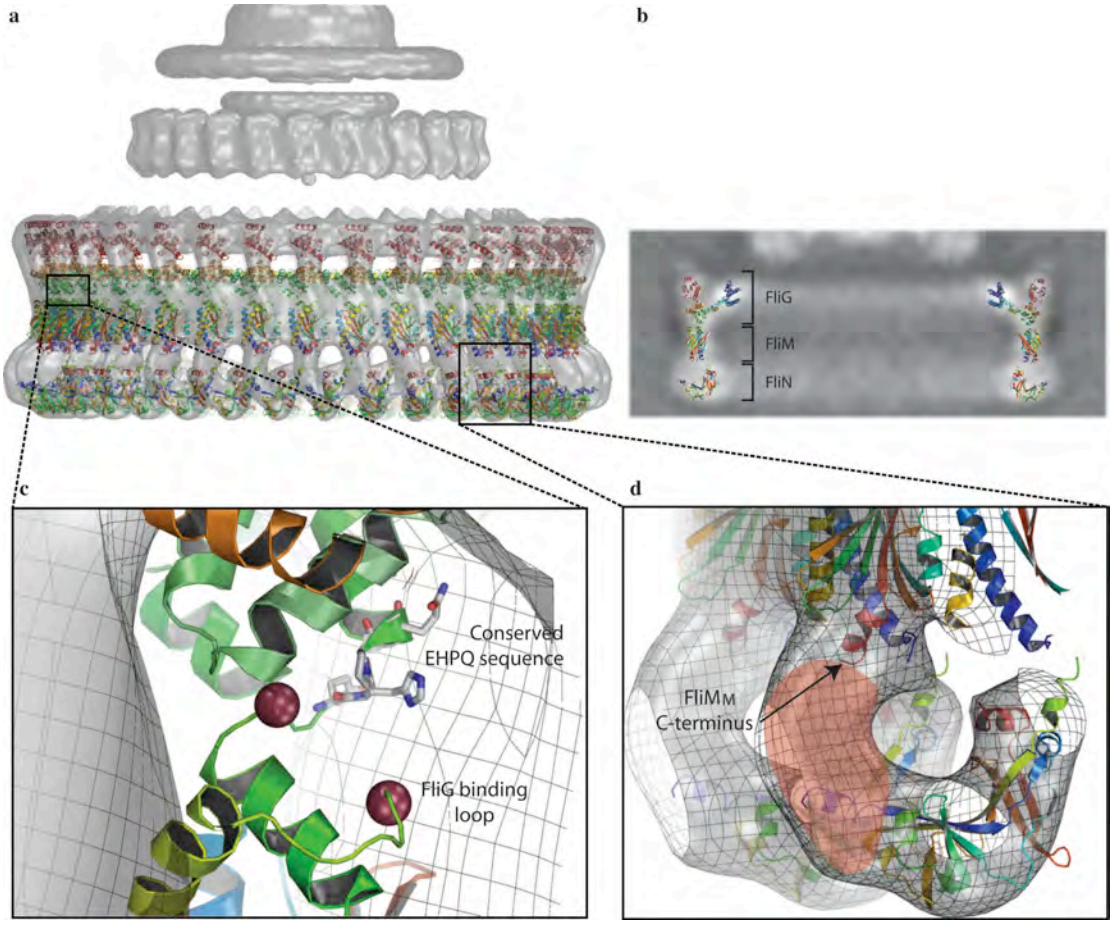

Supplementary Figure 11. Docking of the entire switch complex into the EM density of the C-ring. **a** and **b**, These figures illustrate that the remaining density in the C-ring is sufficiently large to potentially accommodate both the FliM and FliN rings in an arrangement that is consistent with mutagenesis and cross-linking studies. **c**, In the FliG ring, mutations that affect the interaction with FliM on the surface of the ARM superhelix segregate to a single surface on the cytoplasmic side of the ring, pointing towards the remainder of the EM density. After docking the CW FliG ring, we docked the structure of the N-terminal two-thirds of FliM[44] into the EM density with both the FliG-FliM[45,46] and the FliM-FliM[4443] interacting surfaces placed adjacent to each other (**a**-**c**). With these restraints the dimensions of FliM are consistent with the middle third of the C-ring density (**a** and **b**). Furthermore, given the width of the FliM fragment, 34 monomers are required to circumnavigate the C-ring, each with its FliG binding surface in contact with the complementary surface on the FliG ARM superhelix (**a** and **c**) and with a feasible intersubunit spacing of adjacent Cα atoms from neighbouring subunits of around 10 Å. Remarkably, each FliG binding loop aligns with a corresponding EHPQR motif on the ARM superhelix (**c**). The C-terminus of the FliM fragment points towards the base of the C-ring, which forms a right-handed spiral[25], in which the structure of the FliN dimer[47] fits (**a, b** and **d**). The remaining density is large enough to fit another FliN dimer to form a FliN tetramer ring as predicted by cross-linking studies[48] (**d**). Alternatively, since the structurally unknown C-terminal domain of FliM is responsible for binding to FliN[45,49,50] and shares around 25% sequence homology to FliN, which crystallised as a domain-swapped dimer[47], it is tempting to suggest that the remaining spiral density in the base of the C-ring

is formed by a heterodimer consisting of the C-terminus of FliM and a FliN monomer.

Supplementary Movie SM1 Animation detailing the formation of the FliG ring. It starts with a display of the FliG monomer as in Fig. 1a, and continues to highlight key structural features that are important for multimerisation such as the ARM superhelix and intermolecular β-sheet, and finishes detailing how the conformational differences between $FliG_{MC}$ and $FliG_{FL}$ result in a reversal of the torque charges on $helix_{C5}$.

Supplementary Movie SM2 Interpolation of the M236 phi and F237 phi angles between the C-terminal conformations of $FliG_{FL}$ ($Cter_{FL}$) and $FliG_{MC}$ ($Cter_{MC}$). The movie illustrates how $Cter_{FL}$ and $Cter_{MC}$ are related by a 25.6° and 77.8° rotation around M236 phi and M237 phi respectively.

Supplementary Movie SM3 Rotating FliG monomer displaying the equivalent residues at the location of all known rotationally biased mutants. Mutations are shown in stick format and transparent spheres to highlight their clustering around distinct structural regions. CW-biased mutants are in blue, CCW-biased mutants are in yellow and residues where both CW and CCW-biased mutants occur are in green.

Supplementary Movie SM4 Parallels between the ARM_C – ARM_{M+1} right-handed superhelix in the FliG multimer and a eukaryotic ARM superhelix in β-catenin. Like in eukaryotes, the FliG ARM_M and ARM_C motifs contain conserved hydrophobic residues that mediate the hydrophobic stacking of

tandem ARM repeats in adjacent FliG monomers. These form a right-handed superhelix consisting of the seven short helices in the FliG ARM motifs. As is typically seen in ARM superhelices, formation of the β-catenin superhelix creates a surface to mediate interactions with other proteins. We propose that formation of the FliG superhelix is important for FliM binding. This is well supported by mutations that interfere with the ARM_C – ARM_{M+1} interface as these mutations inhibit both flagellar assembly and binding to FliM.

Supplementary Movie SM5 The structure of the $FliG_{UNIT}$. In contrast to the FliG monomer, the C-terminal domain is unlikely to be able to move freely in relation to the rest of the protomer. To illustrate how the $FliG_{UNIT}$ consists of two halves of adjacent FliG monomers, E192 and A193 are labelled. This means that the FliG monomer has to undergo significant conformational changes upon ring formation.

Supplementary Movie SM6 Reversal of the torque generating charges in the FliG ring. The movie displays the transition from the CW $FliG_{MC}$ to the CCW $FliG_{FL}$ states in both directions. Phi and psi torsion angles between the two states were interpolated over 100 frames to create the intermediate states. The top left depicts the conformational changes in the long helices and the C-terminal domain in an individual FliG monomer. The middle and bottom left illustrate the conformational changes in context of the intact ring from the bottom and side view respectively. The colours in the left pane are the same as in Fig. 1 except that E192 and A193 are labelled with yellow and red spheres respectively and the positively (blue) and negatively (red) charged residues on the torque-generating helix are displayed as transparent spheres. The reversal of the positive and negative torque generating charges on the

entire ring is displayed on the right with a single $FliG_{UNIT}$ coloured as in Fig. 1a.

Supplementary References

31 Leslie, A. G. W. *Joint CCP4 and ESF-EACMB Newsletter Protein Crystallography (Daresbury Laboratory, Warrington, UK)* (1992).

32 Collaborative_Computational_Project_Number_4. The CCP4 suite: programs for protein crystallography. *Acta Crystallogr D Biol Crystallogr* **50**, 760-763, (1994).

33 Leahy, D. J., Hendrickson, W. A., Aukhil, I. & Erickson, H. P. Structure of a fibronectin type III domain from tenascin phased by MAD analysis of the selenomethionyl protein. *Science* **258**, 987-991, (1992).

34 Sheldrick, G. M. A short history of SHELX. *Acta Crystallogr A* **64**, 112-122, (2008).

35 Fortelle, E. & Bricogne, G. Maximum-Likelihood Heavy-Atom Parameter Refinement for the Multiple Isomorphous Replacement and Multiwavelength Anomalous Diffraction Methods. *Methods in Enzymology* **276**, 472-494, (1977).

36 Emsley, P. & Cowtan, K. Coot: model-building tools for molecular graphics. *Acta Crystallogr D Biol Crystallogr* **60**, 2126-2132, (2004).

37 Adams, P. D. *et al.* PHENIX: building new software for automated crystallographic structure determination. *Acta Crystallogr D Biol Crystallogr* **58**, 1948-1954, (2002).

38 Davis, I. W. *et al.* MolProbity: all-atom contacts and structure validation for proteins and nucleic acids. *Nucleic Acids Res* **35**, W375-383, (2007).

39 Dolinsky, T. J. *et al.* PDB2PQR: expanding and upgrading automated preparation of biomolecular structures for molecular simulations. *Nucleic Acids Res* **35**, W522-525, (2007).

40 Humphrey, W., Dalke, A. & Schulten, K. VMD: visual molecular dynamics. *J Mol Graph* **14**, 33-38, 27-38, (1996).

41 Suzuki, H., Yonekura, K. & Namba, K. Structure of the rotor of the bacterial flagellar motor revealed by electron cryomicroscopy and single-particle image analysis. *J Mol Biol* **337**, 105-113, (2004).

42 Sowa, Y. *et al.* Direct observation of steps in rotation of the bacterial flagellar motor. *Nature* **437**, 916-919, (2005).

43 Kudryashev, M., Cyrklaff, M., Wallich, R., Baumeister, W. & Frischknecht, F. Distinct in situ structures of the Borrelia flagellar motor. *J Struct Biol*, (2009).

44 Park, S. Y., Lowder, B., Bilwes, A. M., Blair, D. F. & Crane, B. R. Structure of FliM provides insight into assembly of the switch complex in the bacterial flagella motor. *Proc Natl Acad Sci U S A* **103**, 11886-11891, (2006).

45 Mathews, M. A., Tang, H. L. & Blair, D. F. Domain analysis of the FliM protein of Escherichia coli. *J Bacteriol* **180**, 5580-5590, (1998).

46 Passmore, S. E., Meas, R. & Marykwas, D. L. Analysis of the FliM/FliG motor protein interaction by two-hybrid mutation suppression analysis. *Microbiology* **154**, 714-724, (2008).

47 Brown, P. N., Mathews, M. A., Joss, L. A., Hill, C. P. & Blair, D. F. Crystal structure of the flagellar rotor protein FliN from Thermotoga maritima. *J Bacteriol* **187**, 2890-2902, (2005).
48 Paul, K., Harmon, J. G. & Blair, D. F. Mutational analysis of the flagellar rotor protein FliN: identification of surfaces important for flagellar assembly and switching. *J Bacteriol* **188**, 5240-5248, (2006).
49 Marykwas, D. L., Schmidt, S. A. & Berg, H. C. Interacting components of the flagellar motor of Escherichia coli revealed by the two-hybrid system in yeast. *J Mol Biol* **256**, 564-576, (1996).
50 Toker, A. S. & Macnab, R. M. Distinct regions of bacterial flagellar switch protein FliM interact with FliG, FliN and CheY. *J Mol Biol* **273**, 623-634, (1997).